

See discussions, stats, and author profiles for this publication at: <https://www.researchgate.net/publication/233394223>

Adsorption of trimethyl phosphate and triethyl phosphate on dry and water pre-covered hematite, maghemite, and goethite nanoparticles

ARTICLE in JOURNAL OF COLLOID AND INTERFACE SCIENCE · OCTOBER 2012

Impact Factor: 3.37 · DOI: 10.1016/j.jcis.2012.10.012 · Source: PubMed

CITATIONS

8

READS

151

3 AUTHORS, INCLUDING:



Per Persson

Lund University

144 PUBLICATIONS 4,163 CITATIONS

SEE PROFILE

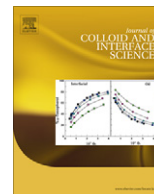


Lars Osterlund

Uppsala University

87 PUBLICATIONS 1,626 CITATIONS

SEE PROFILE



Adsorption of trimethyl phosphate and triethyl phosphate on dry and water pre-covered hematite, maghemite, and goethite nanoparticles

Peter Mäkie^{a,b}, Per Persson^b, Lars Österlund^{a,c,*}

^a FOI, CBRN Defence and Security, SE-901 82 Umeå, Sweden

^b Department of Chemistry, Umeå University, SE-901 87 Umeå, Sweden

^c Department of Engineering Sciences, The Ångström Laboratory, Uppsala University, P.O. Box 534, SE-751 21 Uppsala, Sweden

ARTICLE INFO

Article history:

Received 3 September 2012

Accepted 7 October 2012

Available online xxx

Keywords:

Adsorption

Trimethyl phosphate

Triethyl phosphate

Hematite

Maghemite

Goethite

Diffuse reflectance infrared Fourier transform spectroscopy

X-ray photoelectron spectroscopy

ABSTRACT

Adsorption of trimethyl phosphate (TMP) and triethyl phosphate (TEP) on well-characterized nanoparticles of hematite (α -Fe₂O₃), maghemite (γ -Fe₂O₃), and goethite (α -FeOOH) has been studied by in situ diffuse reflectance infrared Fourier transform spectroscopy (DRIFTS), 2D correlation DRIFTS analysis, and X-ray photoelectron spectroscopy (XPS) on dry and water pre-covered surfaces. It is shown that, at room temperature and low coverage, both TMP and TEP coordinate to Lewis acid Fe sites through the O phosphoryl atom on hematite and maghemite, while hydrogen bonding to Brønsted acid surface OH groups dominates on goethite. At room temperature, slow dissociation of TMP occurs on the iron (hydr)oxide nanoparticles, whereby a methoxy group is displaced to form surface methoxy, leaving adsorbed dimethyl phosphate (DMP). Methoxy is further decomposed to formate, suggesting an oxidative degradation pathway in synthetic air on the oxide particles. Relatively, larger amounts of DMP and surface methoxy form on maghemite, while more formate is produced on hematite. Upon TMP adsorption on dry goethite nanoparticles, no oxidation surface products were detected. Instead, a slow TMP hydrolysis pathway is observed, yielding orthophosphate. It is found that pre-adsorbed water stimulates the hydrolysis of TMP. In contrast to TMP, TEP adsorbs molecularly on all iron (hydr)oxide nanoparticles. This is attributed to the longer aliphatic chain, which stabilizes the loss of charge on the methoxy C–O bonds by charge redistribution upon phosphoryl O coordination to Fe surface atoms. The presented results implicate different reactivity depending on specific molecular structure of the organophosphorus compound (larger functional groups can compensate loss of charge due to surface coordination) and iron (hydr)oxide surface structure (exposing Lewis acid or Brønsted acid sites).

© 2012 Elsevier Inc. All rights reserved.

1. Introduction

Interactions of organophosphorus (OP) compounds with iron and its (hydr)oxides are important in a number of applications, including remediation technologies, catalysis, and environmental fate analysis [1–4]. To date, very few detailed studies have, however, been reported on the interactions of organophosphorus (OP) compounds with iron (hydr)oxides [5,6], which may be related to the relative complexity of these systems. Further, there are only a limited number of studies of other OP/oxide systems. Nanostructured hematite (α -Fe₂O₃) catalyzes the decomposition of pesticides and chemical warfare agents, in particular when stimulated with light [7,8]. It is proposed that clays and iron oxide minerals may be used as catalysts of Fenton-like reactions for the decontamination of soils, groundwater, sediments, and industrial effluents [9]. In environmental sciences, the interaction of OP compounds with

iron (hydr)oxides is important for understanding the bioavailability and degradation of industrial and domestic wastes, pesticides, etc. [8,10–14]. Overload of OP in nature strongly contributes to high levels of anthropogenic phosphate causing eutrophication in soil and water. As a consequence of the high content of iron (hydr)oxides in the earth's crust, and the high reactivity of phosphates toward solid iron-containing particles in terrestrial and aquatic environments [15], iron minerals constitute an important part of the anthropogenic phosphorus cycle. Iron oxides may promote decomposition of OP and can also act as a sink for OP [10]. Furthermore, OP may promote mineral dissolution, regulate available sorption sites, and control sorption of other compounds [16].

An important step toward a comprehensive understanding of OP interactions with iron (hydr)oxides is to devise and study simplified model systems, conducted under idealized conditions, for example, under vacuum or in controlled gas atmosphere, to scrutinize possible elementary steps in the surface chemistry of these systems. Previous studies of such systems include trimethyl phosphate (TMP) adsorption on TiO₂ [17,18], WO₃ [18–20], MgO [21], and α -Fe₂O₃ [22], respectively, and triethyl phosphate (TEP)

* Corresponding author at: Department of Engineering Sciences, The Ångström Laboratory, Uppsala University, P.O. Box 534, SE-751 21 Uppsala, Sweden.

E-mail address: lars.osterlund@angstrom.uu.se (L. Österlund).

adsorption on TiO₂ [17] and MgO [21], respectively. In addition, there are several studies on model phosphonates, such as dimethyl-methyl phosphonate (DMMP), on well-defined metal oxide systems, in particular TiO₂ [23,24], and also on iron oxides [8]. Similar model studies of OP interactions with iron (hydr)oxides are hitherto by and large lacking [6].

In the present study, we employ three distinct, well-characterized forms of iron (hydr)oxide colloidal particles [6]: hematite (α -Fe₂O₃), maghemite (γ -Fe₂O₃), and goethite (α -FeOOH), respectively, as model systems for OP interaction with iron (hydr)oxide in synthetic air. We use two simple OP compounds, TMP and TEP, which differ only by the length of the aliphatic chain. These OP constitute the basic structures of many pesticides [10]. We employ in situ diffuse reflectance infrared Fourier transform spectroscopy (DRIFTS) and X-ray photoelectron spectroscopy (XPS) to study the gas-phase OP adsorption on iron oxide nanoparticles, with and without pre-adsorbed water in synthetic air. The inclusion of water vapor aims to simulate an intermittent situation between adsorption at the gas–solid and liquid–solid interfaces.

2. Experimental

2.1. Materials

The preparation of oxide and hydroxide nanoparticles and their physical properties have been reported in a previous publication [6]. The samples were pre-treated prior to experiments to remove organic residues as determined by DRIFT spectroscopy as follows: Maghemite samples were calcined at 300 °C for 80 min and washed in 4 mM NaOH and milliQ-water to remove organic residues [25]. The hematite and goethite samples were in addition annealed in situ in the reaction cell at 400 and 200 °C, respectively, for 20 min in synthetic air and then cooled to 20 °C. The lower annealing temperatures for maghemite and goethite were necessary to ensure phase purity. Phase purity (determined by Raman spectroscopy) and spectroscopic purity of the samples (determined by in situ DRIFT during pre-treatment) were confirmed prior to measurements. The physical properties of the nanoparticles are summarized in Table 1 [6]. The OP compounds trimethyl phosphate (liquid TMP; C₃H₉O₄P) (98% GC purity, Merck Germany) and triethyl phosphate (liquid TEP; C₆H₁₅O₄P) (98% GC purity, Sigma-Aldrich, USA) were used without further purification.

2.2. Diffuse reflectance infrared Fourier transform spectroscopy

In situ Diffuse Reflectance Infrared Fourier Transform spectroscopy (DRIFTS), measurements were performed in a modified reaction cell using a Bruker IFS-66v/S spectrometer equipped with

Table 1
Physical properties of iron oxide and hydroxide nanoparticles.

Material	<i>d</i> (nm) (TEM)	<i>d</i> (nm) (XRD)	Fe/O ratio (XPS)	BET surface area (m ² g ⁻¹)	BJH average pore width (nm)
Hematite	~30	30.74 ^d	2:3.031	28.98	22.2
Maghemite	~20 (~35) ^a	16 ^e	2:2.931	90.03	7.9
Goethite	~11 ^b ~62 ^c	8.06 ^f 31.83 ^g	1:981	100.06	13.6

^a Value in parenthesis shows the average *d* determined for the (sedimented) large particles.

^b Average calculated as an average of height and width.

^c Average calculated from length of long-axis.

^d Average calculated from the (012), (104), (110), (116) reflections

^e Average calculated from the (220), (311), (400) reflections.

^f Average calculated from the (110) reflection.

^g Average calculated from the (002) reflection.

liquid nitrogen-cooled broad-band MCT detector. Spectra were acquired at 4 cm⁻¹ resolution, and each spectrum was the average of 128 scans. Repeated in situ DRIFT spectra were acquired as a function of dosing time with background spectra acquired in synthetic air ~6 min before introduction of TMP and TEP. The reported spectra are raw spectra without any smoothing or baseline corrections. The DRIFT reaction cell was connected to a gas generator system, which allows controlled dosing of reaction gas in the reaction cell as described elsewhere [25]. Briefly, the reaction gas was generated by evaporation of OP liquids into a carrier gas stream (synthetic air, 100 ml min⁻¹) from a diffusion tube connected to a temperature controlled reservoir held at $T = 62 \pm 0.2$ °C, yielding a gas injection rate of 6.08 and 2.56 $\mu\text{g min}^{-1}$ into the feed gas for TMP and TEP, respectively (equivalent to 19 ppbv and 6 ppbv, respectively). This low dose rate was chosen to be able to explore sub-monolayer adsorption with sufficient time-resolution in the in situ experiments. In experiments with pre-adsorbed water, the samples were exposed to humidified air (relative humidity, RH 17%) for 20 min, followed by 20 min of dry synthetic air (purging). This corresponds roughly to an initial water coverage on the surfaces of ca. 4 monolayers (MLs), assuming that the water desorption energy is equal to the sublimation energy. Here, 1ML of water is defined to be 10¹⁹ molecules m⁻². To ensure reproducibility, the water exposure was simultaneously measured by in situ DRIFTS. A rough estimate assuming zero order desorption showed that 0.5% of the water coverage desorbs during the purging period (20 min). OP dosing was then performed in the same manner as in the dry experiments. Liquid reference spectra of OP liquids were acquired using a DuraS-amplIRII ATR accessory equipped with a nine internal reflection diamond element and collected at 2 cm⁻¹ resolution. Each spectrum was averaged over 300 scans and corrected for the wavelength dependent intensity [26].

2.3. 2D correlation analysis

DRIFT spectra were analyzed with 2-dimensional (2D) correlation analysis using the 2Dshige program [27] following the general procedures described by Noda and Ozaki [28]. Spectral 2D correlation was analyzed as a function of OP dosing time (external perturbation). The analysis was performed in the methyl stretching region between 3050 and 2790 cm⁻¹ and in the finger print region between 1600 and 1000 cm⁻¹. The spectra were baseline corrected by fitting straight lines between the endpoints of each region. From the 2D correlation analysis, correlated and uncorrelated spectral variations were identified, as well as the time-sequences of absorbance variations. This facilitated assignments of vibrational bands associated with uncorrelated species, and their temporal evolution as a function of OP dosing time, which were used to construct kinetic models of OP reactions on the (hydr)oxide particles. Detailed description of the 2D correlation analysis is provided in the Supporting information.

2.4. Kinetic modelling

Kinetic models were constructed based on the temporal evolution of the concentrations of uncorrelated surface species obtained from DRIFTS and 2D correlation analysis. Parameter fitting of the kinetic models was performed using iterative numerical integration over the time interval $0 \leq t \leq 42$ min, defined by the discrete time step, t_i , using the Matlab ODE Runge–Kutta solver, ode45. For each DRIFT spectrum, the root means square, rms , function, $rms \sum_i \sqrt{\sum_i (\theta_i(t_i) - \hat{\theta}_i(t_i))^2}$, was minimized over the parameter space defined by the uncorrelated species, where j is the OP rate constants for adsorption and reactions, θ_j is the surface coverage of specie j at time t_i obtained from numerical integration, and $\hat{\theta}_j$

is the corresponding experimental data obtained from DRIFTS. Conversion and calibration of DRIFT absorbance ($\log(1/R)$) to absolute concentration as a function of dosing time for the $\nu(\text{P=O})$ and $\nu_{\text{a}}(\text{C—O—(P)})$ TMP bands were done as described before [6]. In the analysis, the TMP $\nu_{\text{a}}(\text{C—O—(P)})$ band at $\sim 1050\text{ cm}^{-1}$ was used, where 1 $\log(1/R)$ unit corresponds to 1.08×10^{21} molecules m^{-2} . We assume that the corresponding $\nu(\text{P—O})$ band for the DMP adducts (from TMP dissociation) obey the same calibration (i.e., has the same IR cross section), and the experimental coverage of DMP is multiplied by the factor 3/2 for stoichiometric reasons. We have, however, no a priori knowledge about the absolute surface coverage of, for example, hydroxyl, methoxy, or formate surface species. Instead, we include a numerical factor in the simulations to take into account differences in IR cross sections, in the instances where such species are present in the kinetic models. The presented surface coverage is normalized to the TMP $\nu_{\text{a}}(\text{C—O—(P)})$ band at 1050 cm^{-1} at $t_i = 42$ min and corresponds to 4.8, 2.3, and 1.8 ml on hematite, maghemite and goethite, respectively, using reported values for their specific surface area [6], and where 1 ml of TMP is defined to be 2.6×10^{18} molecules m^{-2} using the van der Waals radius for TMP (3.5 Å).

2.5. X-ray photoelectron spectroscopy

X-ray photoelectron spectroscopy (XPS) characterization was performed with a Kratos Axis Ultra electron spectrometer using a monochromatic Al K α X-ray source operated at 150 W, a hybrid lens system with magnetic lens, and a charge neutralizer. Both wide spectrum (pass energy 160 eV) and narrow scans of all detected elements (pass energy 20 eV) were acquired. The binding energy (BE) scale was referenced to the C1s line of aliphatic carbon set at 285.0 eV. Processing of the spectra was accomplished with Kratos software and the CasaXPS program package [29].

3. Results

Fig. 1 shows in situ DRIFT spectra of TMP and TEP adsorbed on hematite (Fig. 1a), maghemite (Fig. 1b), and goethite (Fig. 1c), respectively, as a function of OP dosing time (0, 6, 12, 22, 32, and 44 min). According to the absolute coverage calibration, the spectra obtained at $t < 12$ min represent OP coverage in the sub-monolayer regime on hematite, while spectra at $t < 20$ min represent sub-monolayer coverage on maghemite and goethite (Fig. S1, Supporting information). Multilayer adsorption contributes to the observed DRIFT spectra at long dosing times, and we will therefore focus on the sub-monolayer coverage regime here to scrutinize the OP-oxide interactions. By comparisons with ATR-FTIR spectra obtained on pure TMP and TEP liquids (Fig. S2a, Supporting information), it is evident that molecular TMP and TEP are the main species, which gradually accumulate on the surfaces. In particular, the strong bands at $\sim 1050\text{ cm}^{-1}$ and $\sim 1030\text{ cm}^{-1}$ are due to the $\nu_{\text{a}}(\text{C—O—(P)})$ mode in TMP and TEP, respectively. Large downshifts of the $\nu(\text{P=O})$ stretching frequency are observed on all surfaces (Table 2). This is due to bonding of the OP phosphoryl O atom (Lewis base) to a cation surface site (Lewis acid) with concomitant charge depletion of the P=O bond [6,8,19,30]. On goethite, a doublet $\nu(\text{P=O})$ band is observed for both TMP and TEP, which previously has been attributed to two different species; one species which bonds to the surface through a phosphoryl O—Fe bond, and one species which is hydrogen bonded to surface hydroxyls [6]. The former assignment is supported by a recent study of TMP adsorption on single crystal $\alpha\text{-Fe}_2\text{O}_3(012)$ [22]. Closer inspection of the DRIFT spectra for TMP adsorption (Fig. 1, lower panels) reveals that new, minor absorption bands appear on all iron (hydr)oxide particle surfaces as a function of dosing time, which can-

not be assigned to TMP. A 2D correlation analysis shows that the new absorption bands at ~ 1050 , ~ 1080 and $\sim 2820\text{ cm}^{-1}$ originate from independent surface species (Figs. S3–S5, Supporting information). By comparisons with previous studies, we attribute the 1080 cm^{-1} band to the $\nu(\text{P—O})$ mode in dimethyl phosphate (DMP) [31,32] and the 2820 cm^{-1} band to the characteristic $\nu_{\text{s}}(\text{C—H})$ surface methoxy [8,23,33–36], which shows that TMP dissociates on the iron (hydr)oxide nanoparticles. The reference spectrum of DMP in aqueous solution is shown in Fig. S2b, Supporting information.

Furthermore, the signs of the asynchronous correlation of the absorption bands show that the species develop in the sequence TMP, DMP, and finally methoxy (Figs. S3–S5, lower panels, Supporting information). On hematite, absorption bands due to coordinated formate species are also observed [6,23,34,37–40]. Corresponding bands on the other samples are very weak (maghemite) or absent (goethite). This suggests that surface methoxy eventually becomes oxidized (hematite). On goethite, a new absorption band appears at 1146 cm^{-1} after an initial dwell time that can be assigned to surface coordinated orthophosphate [41,42], which is supported by the 2D correlation analysis showing that this reaction occurs after DMP formation. The absence of intermediate species, such as formate which is observed on hematite, suggests that displaced methoxy fragments desorb from goethite (and presumably also maghemite), possibly as methanol, as previously has been reported [43,44]. The vibrational bands of the dissociation products and their mode assignments are shown in Table 3.

In contrast to TMP, the spectra for TEP in Fig. 1 (upper panels) show that TEP does not dissociate on any of the oxide surfaces, albeit the weak shoulders at $\sim 1070\text{ cm}^{-1}$ may be assigned to the $\nu_{\text{s}}(\text{CO})$ band in diethyl phosphate (DEP) [45]. However, this band is also discernible in the spectrum of neat TEP and may be indicative of minute levels of hydrolysis in the start material. Both TMP and TEP adsorption result in displacement of surface hydroxyls as evidenced by the negative absorption bands in the $3600\text{--}3700\text{ cm}^{-1}$ region. On goethite, the characteristic band due to lattice OH at $\sim 3490\text{ cm}^{-1}$ decreases, in agreement with previous reports [6], supporting the assignment above of two types of OP adsorption sites on goethite: Lewis acid (Fe cations) and Brønsted acid (surface terminated lattice OH associated with the 3490 cm^{-1} band), respectively, and a concomitant splitting of the $\nu(\text{P=O})$ band. The slight increase in the water bands at $3200\text{--}3500\text{ cm}^{-1}$ is due to weak background absorption of trace amount of water present in the reaction gas, which is always the case for high-pressure studies of dehydrated, hygroscopic oxides.

Fig. 2 shows in situ DRIFT spectra acquired during adsorption of TMP and TEP on (hydr)oxide surfaces pre-adsorbed with water. TMP and TEP displace water as seen by the depletion of the water absorption bands. Similar to dry surfaces, TEP does not dissociate on water pre-covered surfaces. However, in the case of TMP, the effect of water depends on the specific sample. Fig. 3 shows the DMP concentration as function of dosing time normalized to the TMP $\nu(\text{C—O—P})$ bands on dry and water pre-adsorbed nanoparticles. This normalization facilitates intra sample comparisons, as it removes differences in surface area and reflectivity evident in Figs. 1 and 2.

It is evident from Fig. 3 that the amount of adsorbed DMP in the sub-monolayer regime ($t < 12$ min for hematite, and $t < 20$ min for maghemite and goethite) on the dry oxides corresponding to Fig. 1 increases in the order: hematite \ll goethite $<$ maghemite. On water pre-covered surfaces, the relative concentration of DMP generally increases, and in the sub-monolayer regime, it increases in the order: hematite \sim maghemite $<$ goethite.

Fig. 4 shows the absorbance ($\log(1/R)$) vs. dosing time of the $\nu_{\text{a}}(\text{P—O})$ bands at 1145 and 1165 cm^{-1} due to orthophosphate on dry and water pre-adsorbed goethite, respectively, normalized to

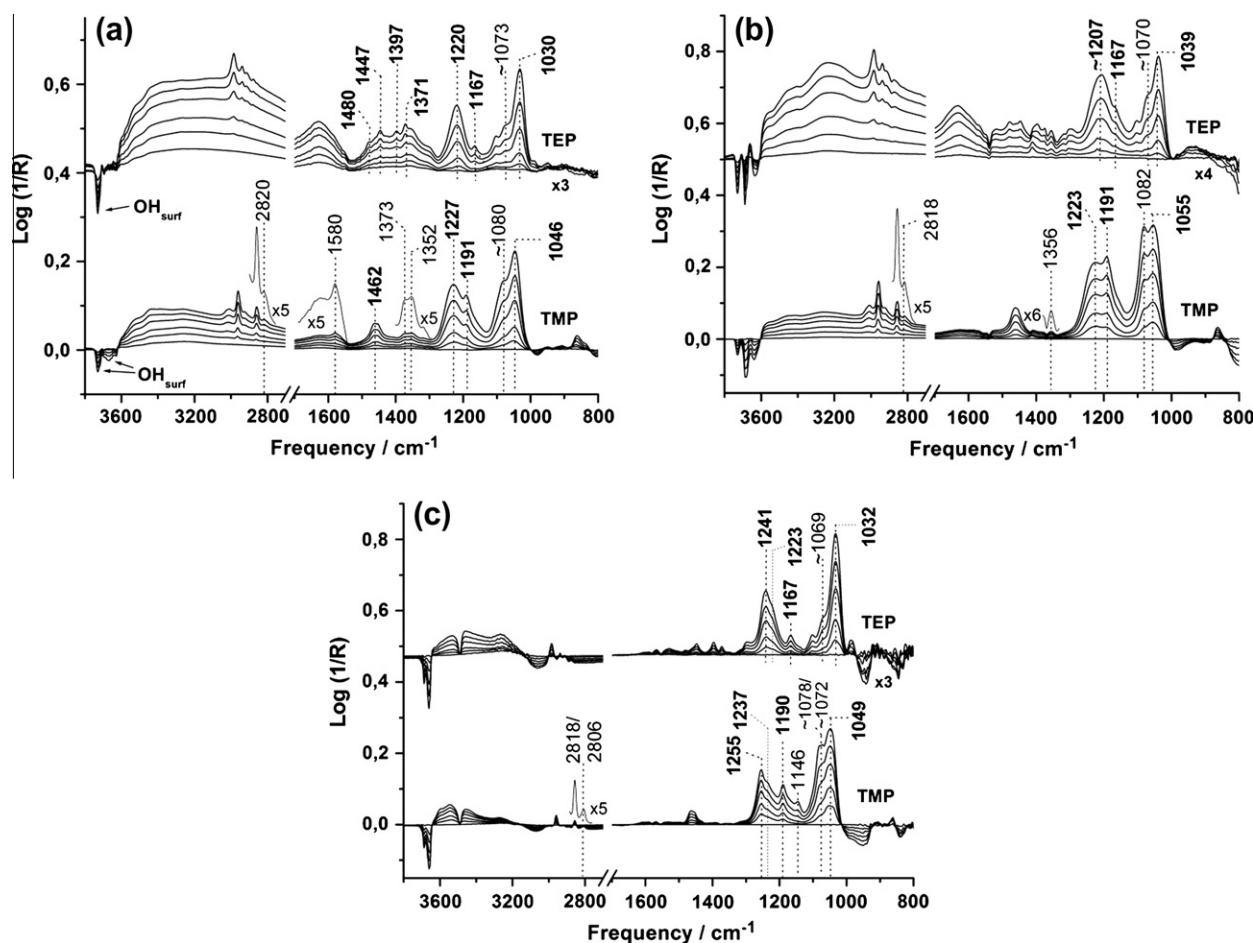


Fig. 1. Adsorption of TMP and TEP on (a) hematite, (b) maghemite, and (c) goethite at different times during gas dosing (bottom to top: 3, 21 and 48 min dosing time).

Table 2
Compilation of $\nu(\text{P}=\text{O})$ stretching frequencies (in cm^{-1}) of TMP and TEP adsorbed on dry and water pre-covered hematite (Hem/HemW), maghemite (Magh/MaghW) and goethite (Goeth/GoethW), respectively. The corresponding frequencies for TMP and TEP liquids measured with ATR-FTIR are also shown.

	Mode	Hem	HemW	Magh	MaghW	Goeth	GoethW	Liquid
TMP	$\nu(\text{P}=\text{O})$	1227	1235	1223	1220	1255/1237	1246	1278/1268
TEP	$\nu(\text{P}=\text{O})$	1220	1219	1207	1204	1241/1223	1231	1271/1261

For goethite, a 2D correlation analysis shows that the doublet $\nu(\text{P}=\text{O})$ bands at $\sim 1080 \text{ cm}^{-1}$ and $\sim 1072 \text{ cm}^{-1}$, and the doublet $\nu_s(\text{C}-\text{H})$ at 2818 and 2807 cm^{-1} , originate from same species (DMP and surface methoxy, respectively). The characteristic methoxy $\nu(\text{C}-\text{O})$ band at $\sim 1030 \text{ cm}^{-1}$ is obscured by the strong TMP and DMP bands in this region, but can be noticed in the asynchronous correlation plots (Fig. S5, Supporting information).

Table 3
Infrared bands (in cm^{-1}) and mode assignments of TMP dissociation products on iron oxide and hydroxide nanoparticles.

Hematite		Maghemite		Goethite		Assignment
Dry	Wet	Dry	Wet	Dry	Wet	
2820	2806	2818	2817	2818/2806		$\nu_s(\text{CH})^a$
1580	–	–	–	–	–	$\nu_{as}(\text{O}-\text{C}-\text{O})^b$
1373	–	–	–	–	1377	$\nu_s(\text{O}-\text{C}-\text{O})^b$
1352	1347	1356	1358	–	1355	$\nu_s(\text{O}-\text{C}-\text{O})^b$
–	–	–	–	1146	1165	$\nu_a(\text{P}-\text{O})^c$
1080	1084	1082	1080	1080/1072		$\nu(\text{P}-\text{O})^d$

^a Surface methoxy species.

^b Coordinated formate species.

^c Orthophosphate from the present study and reported $\nu_{3,a}(\text{P}-\text{O})$ vibration of solution $(\text{HO})_3\text{P}=\text{O}$ and $(\text{HO})_2\text{PO}_2^-$, respectively [43].

^d Coordinated DMP from the present study and reported $\nu_s(\text{P}-\text{O})$ combination vibration of solution $(\text{OCH}_3)_2\text{PO}_2^-$ [31].

the $\nu_a(\text{C}-\text{O}-\text{P})$ bands due to TMP. A rough estimate shows that the surface concentration of orthophosphate species approaches $\sim 20\%$ of the DMP coverage after 45 min adsorption, assuming that the infrared cross sections of the $\nu(\text{P}-\text{O})$ band in DMP and H_2PO_4 are similar. It is evident that the relative concentration of orthophosphate compared to DMP is larger on water covered goethite, pointing to a dominant DMP hydrolysis mechanism for TMP dissociation on goethite.

Fig. 5 displays XPS P 2p spectra obtained after gas-phase exposure to TMP at different substrate temperatures. In all cases, the P 2p spectra were fitted with doublet constraints: A fixed spin-orbital splitting of 0.84 eV and a fixed P 2p_{3/2}: P 2p_{1/2} intensity level of 2:1. Measurements were performed at cryogenic temperatures (118 K) on neat TMP, hematite, and goethite. At 118 K (panel I), both chemisorbed and physisorbed OP species are observed. After evacuation at 295 K, the weakly bonded (physisorbed) TMP molecules are almost completely removed (panel II). Only chemisorbed species remain with characteristic BE corresponding to OP species (Table 4).

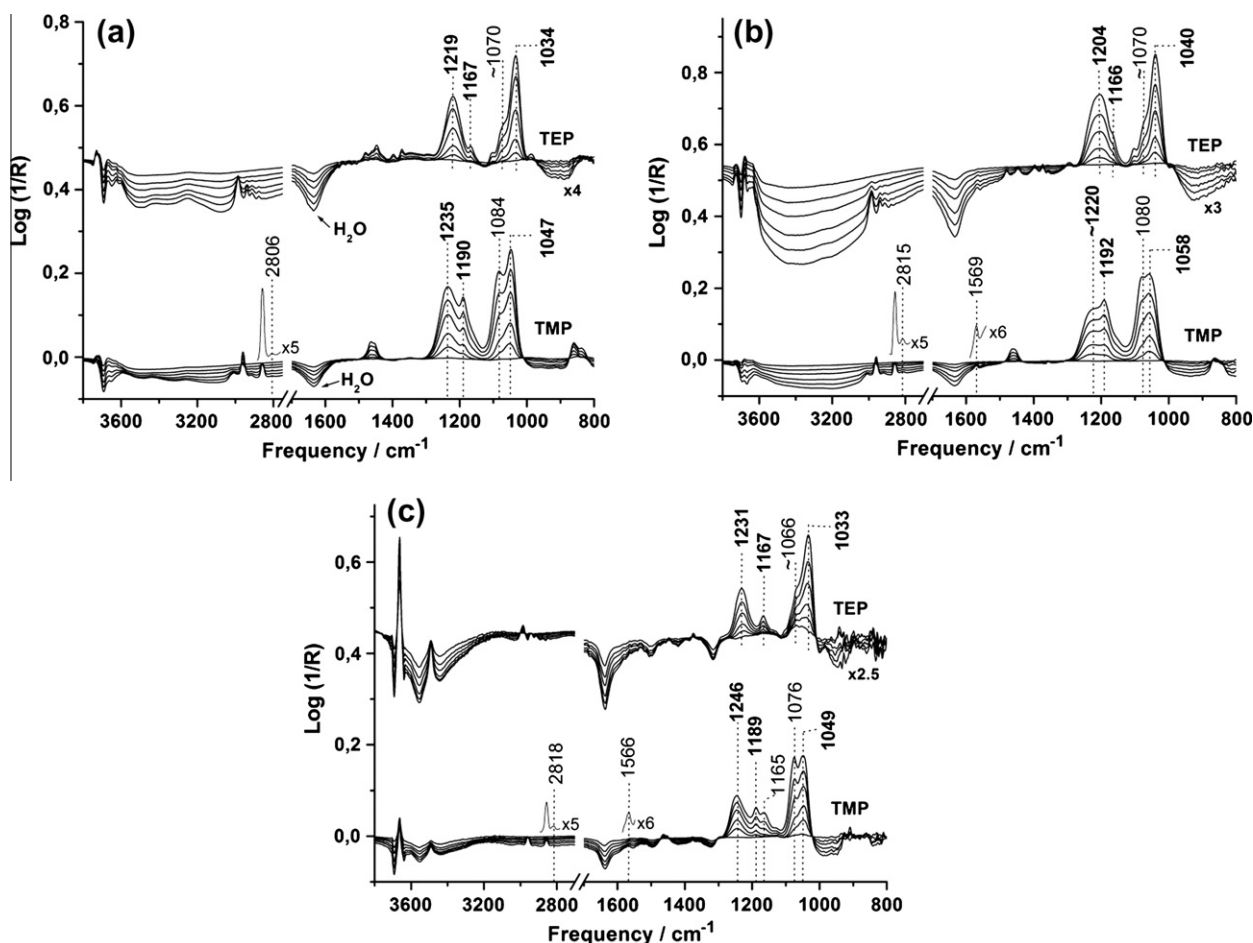


Fig. 2. In situ DRIFT spectra obtained at different times during OP adsorption on (a) hematite, (b) maghemite, and (c) goethite nanoparticles, respectively, pre-adsorbed with water (bottom to top: 3, 21 and 48 min dosing time).

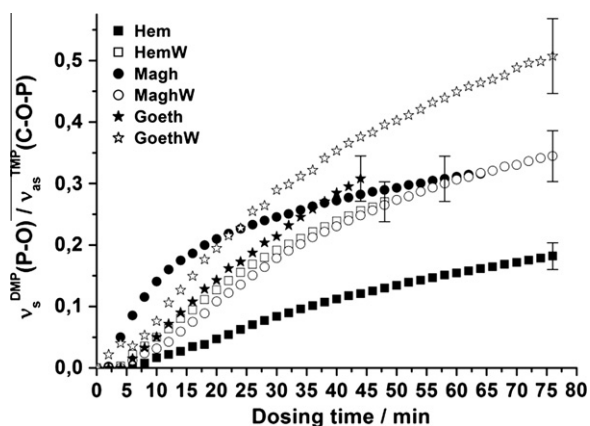


Fig. 3. Absorbance (log(1/R)) vs. dosing time of the DMP $\nu_s(\text{P-O})$ bands at ~1080 cm⁻¹ (sum of ~1080 and 1072 cm⁻¹ bands for dry goethite) normalized to the TMP $\nu_s(\text{P-O})$ band at 1050 cm⁻¹. The black and gray markers represent adsorption on dry and pre-covered ("W") surfaces, respectively. The error bars represent 12% of experimental data.

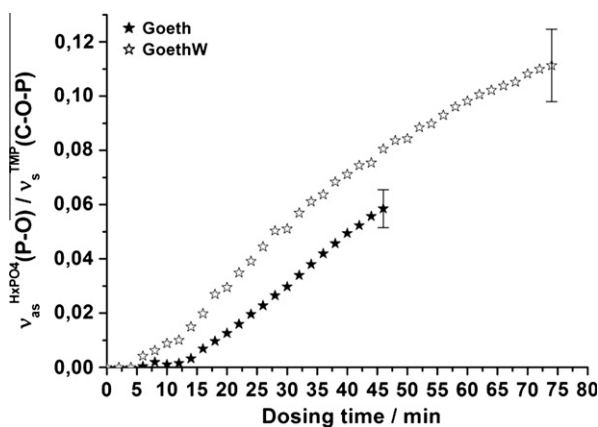


Fig. 4. Absorbance (log(1/R)) vs. dosing time of the orthophosphate $\nu_{\text{as}}(\text{P-O})$ bands at 1145 and 1165 cm⁻¹ acquired during TMP adsorption on dry and water pre-covered ("W") goethite. The data are normalized to the TMP $\nu(\text{C-O-P})$ band at ~1050 cm⁻¹. The error bars represent 12% of experimental data.

A quantitative analysis reveals that the relative concentration of chemisorbed OP species is higher on hematite and maghemite compared to goethite (Table 5). This is in good agreement with the DRIFTS data, which shows that coordinated TMP (chemisorbed) species preferentially form on the oxides, while a significant amount of TMP is hydrogen bonded on goethite. Similarly, in

Table 5 is also shown that the OP derived C 1s concentration due to the methoxy groups is lower compared to the corresponding liquid, which further proves that methoxy are displaced and eventually desorb from the surfaces to a higher extent on goethite compared to the oxides in good agreement with DRIFTS. On goethite, small amounts of inorganic phosphate species can be

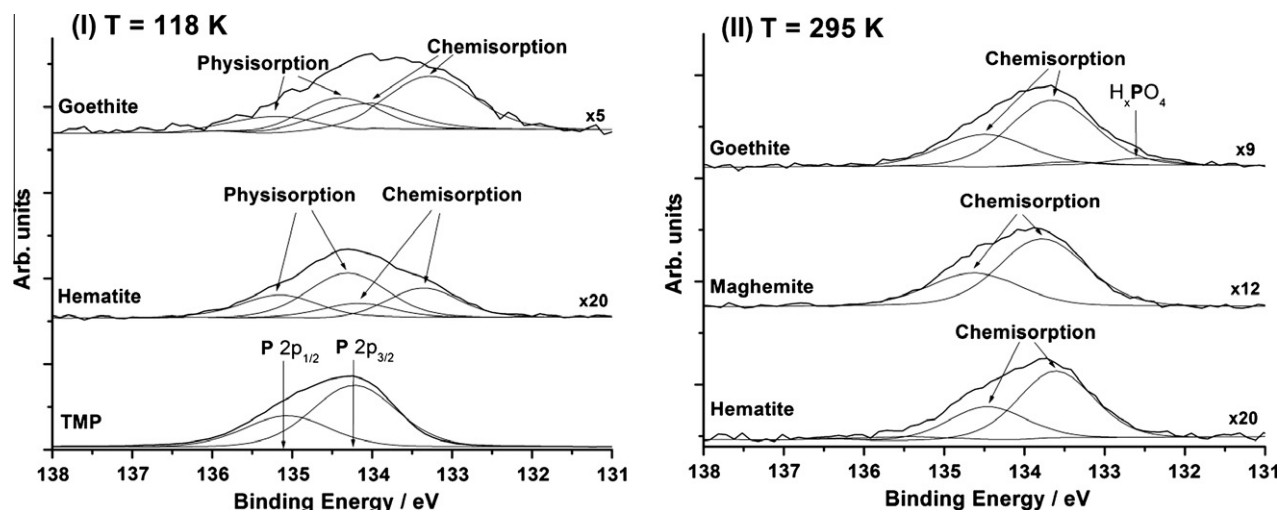


Fig. 5. Panel I: XPS P 2p spectra acquired at 118 K of liquid TMP (bottom), and TMP adsorbed on nanopowders of hematite (middle) and goethite (top). Panel II: XPS P 2p spectra of TMP adsorbed at 295 K on nanopowders of hematite (bottom), maghemite (middle) and goethite (top).

Table 4
XPS P2p and C1s binding energies (BE) for different iron oxide samples exposed to TMP vapor at different substrate temperatures. Corresponding data for liquid TMP are shown for comparison ("Ref").

Assignment	Hematite, BE (eV)		Maghemite, BE (eV)	Goethite, BE (eV)		Ref., BE (eV)
T_{sample}	118 K	295 K	295 K	118 K	295 K	118 K
P 2p _{3/2} (H ₃ PO ₄)	–	–	–	–	132.6	–
P 2p _{3/2}	133.3	133.6	133.8	133.3	133.7	–
P 2p _{1/2}	134.0	134.4	134.6	134.1	134.5	–
P 2p _{3/2}	134.4	–	–	134.3	–	134.2
P 2p _{1/2}	135.2	–	–	135.2	–	135.1
C 1s (CH ₃ O)	287.2	287.0	286.8	286.9	286.8	287.1

identified by a peak at BE = 132.6 eV. Again, this is in perfect agreement with the occurrence of orthophosphate surface species in the DRIFT spectra (Figs. 1c, 2c and 5, panel II).

Fig. 6 shows XPS C 1s spectra of a rapidly frozen liquid TMP drop acquired at low temperature (118 K). This is compared with corresponding XPS spectra of TMP adsorbed at room temperature on the (hydr)oxide nanoparticles. Apart from the dominant C species due to the methoxy moieties, a weak characteristic C 1s shoulder originating from carbonyl species is discernible at BE = 288.5 eV on hematite and maghemite, which is absent on goethite. This is consistent with the DRIFTS data, which show that formate (carboxylate) species form on the hematite and maghemite nanoparticles, but not goethite.

4. Discussion

The results above show that TMP and TEP react very differently on the iron (hydr)oxide nanoparticles. Slow TMP dissociation is observed on all samples at room temperature, in agreement with previous studies [6,22], while TEP does not dissociate on any sample (we assign the trace amounts of DEP which are seen in the DRIFT spectra to presence of minor hydrolysis products in the neat TEP, Fig. SI2a, Supporting information). Furthermore, the reactivity is different on the different particles. A broad distinction can be made, where the oxide nanoparticles (hematite and maghemite) show different TMP surface coordination and product distribution compared to the hydroxide (goethite) nanoparticles. Previously, we [6] and others [8,22] reported that the large red-shift in the $\nu(\text{P}=\text{O})$ mode observed on the oxides can be attributed to bonding

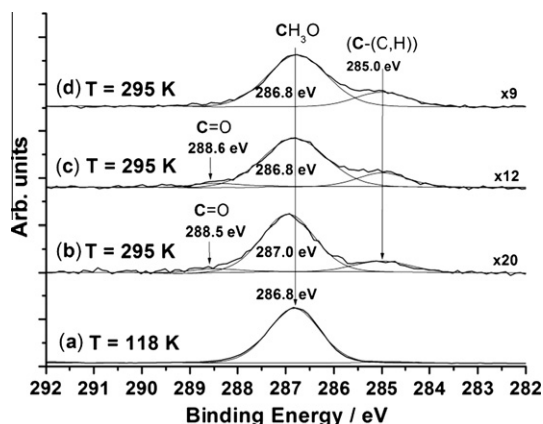
of the phosphoryl O atom in TMP to Fe cation surface atoms, which results in a weakening of the internal TMP bonds. A similar or even larger down-shift of the (P=O) frequency is seen for TEP as for TMP (Table 1). This may appear contradictory, since this down-shift is believed to be the reason for TMP dissociation as inferred from simple valence bond representation. Bonding of the phosphoryl O atom to a surface Fe cation leads to charge redistribution within TMP, where the P–O–(C) bond order increases and the corresponding $\nu_{\text{a}}(\text{C}=\text{O}-\text{P})$ frequency increases, while at the same time, the O–C bonds are weakened. The increased $\nu_{\text{a}}(\text{C}=\text{O}-\text{P})$ frequency has been reported before [6] and is also apparent in Figs. 1 and 2. In TEP, it appears that the longer C–C chain can compensate this, presumably by π charge delocalization. Similar arguments have been previously been put forward for other adsorption systems [46]. A more complete description must, however, consider the energetics of the full reactions to analyze the contribution from the leaving group. For example, considering the hydrolytic surface reactions of TMP and TEP, that is, $\text{TMP}_{\text{ad}} + \text{OH}_{\text{ad}} \rightarrow \text{DMP}_{\text{ad}} + \text{MeO}_{\text{ad}}$ and $\text{TEP}_{\text{ad}} + \text{OH}_{\text{ad}} \rightarrow \text{DEP}_{\text{ad}} + \text{EtO}_{\text{ad}}$, where DEP is diethyl phosphate. Here, comparisons can be made with corresponding density functional theory (DFT) calculations of the hydrolysis of aqueous TMP [47]. These DFT calculations show that methoxy is a poorer leaving group compared to larger aliphatic and aromatic functional groups. This is in contrast to our observations, which show the reversed trend, and therefore indicates that surface mediated reactions, which involve cation coordinated species, are different from bulk hydrolysis reactions.

Gas-phase adsorption on hematite in synthetic air results in significant amounts of surface formate species compared to maghemite (little) and goethite (absent). On maghemite and goethite,

Table 5

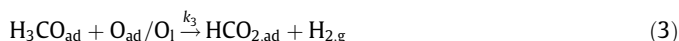
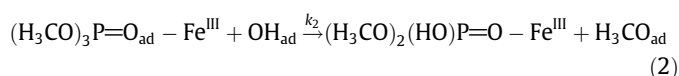
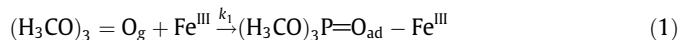
Atomic ratios deduced from XPS. Substrate temperature is indicated in parenthesis.

Atomic ratio	Hem + TMP	Magh + TMP	Goeth + TMP	TMP liq.
P 2p (chemisorbed/physisorbed) (118 K)	1.8	–	0.6	–
C 1s (OCH ₃)/P 2p (<i>P</i> _{tot}) (295 K)	2.8	2.8	2.7	3.1
P 2p (HPO ₄ ^{2−})/P 2p (<i>P</i> _{tot}) (295 K)	–	–	0.04	–
C 1s (C=O)/C 1s (<i>C</i> _{tot}) (118 K)	0.08	–	–	–
C 1s (C=O)/C 1s (<i>C</i> _{tot}) (295 K)	0.06	0.04	–	–

**Fig. 6.** XPS C 1s spectra of fast-frozen liquid TMP drop taken under liquid nitrogen cooling (118 K) (a) and TMP adsorbed at room temperature (295 K) onto the nanopowders of hematite (b), maghemite (c), and goethite (d).

the relative amounts of DMP to TMP are higher than that on hematite (Fig. 3). On all samples, surface methoxy and formate formation are suppressed by pre-adsorbed water. Moreover, on goethite, a slow orthophosphate formation pathway is identified that is stimulated by the presence of pre-adsorbed water (Fig. 4). These observations indicate that formate formation mainly originate from oxidation of the methoxy fragment that is displaced when Fe coordinated TMP dissociates to form DMP and not due to further decomposition of DMP. The DRIFTS data suggest that Fe cation coordinated DMP is stable under the time-scale of the experiments. Instead, we propose a slower hydrolysis pathway, which occurs in parallel and which is responsible for the decomposition of hydrogen bonded DMP on goethite to yield orthophosphate.

Fig. 7 summarizes the proposed reaction mechanisms. In Fig. 7a, the following reaction steps are identified on dry oxide particles (hematite and maghemite):



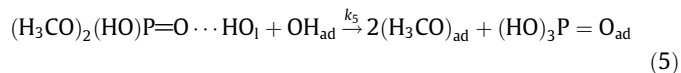
Here, O_l and O_{ad} denote possible oxygen atoms: lattice O or adsorbed O, respectively. The reaction involving surface OH on “dry” oxide surfaces is evidenced by the negative hydroxyl bands in the DRIFT spectra in Fig. 1. As mentioned above, this is due to gradual re-hydroxylation of the in situ annealed surfaces and occurs in the gas flow prior to the OP adsorption experiments. Reaction (1) is the TMP adsorption step, whereby the phosphoryl O atom binds to a surface Fe cation site (identified by DRIFTS and XPS). In reaction 2, a TMP methoxy group is displaced, and a Fe(III) coordinated DMP specie forms (identified by DRIFTS, XPS, and supported by previous

reports [6,22]). Reaction (3) describes oxidation of surface methoxy to surface formate (evidenced by DRIFTS and XPS). It is evident from the DRIFTS data that the surface formate formation cannot be the sole reaction pathway for the displaced methoxy, since it is absent on goethite and minute on maghemite.

Thus, desorption of displaced methoxy fragments are indirectly inferred from DRIFT and XPS data to account for mass balance, viz.



This is supported by the recent study by Henderson [22], and previous reports on DMMP reaction with other metal oxides [48,49]. From DRIFTS data, it is clear that reaction 3 dominates at low coverage on hematite, and that reaction 4 dominates on goethite. With pre-adsorbed water, the reactions are shifted toward reaction 4 on all surfaces. Fig. 7b depicts the hydrolysis reaction, which is proposed to be dominant on goethite. To account for orthophosphate formation (evidenced by DRIFTS and XPS), which primarily occurs on goethite, a hydrolysis reaction involving hydrogen bonded DMP is introduced, viz.



To further quantify the TMP reactions, a kinetic model was constructed based on the uncorrelated surface species determined from DRIFTS and 2D correlation analysis. The following bands originating from TMP, DMP, and surface methoxy were used in the analysis: TMP $\nu_{\text{a}}(\text{P}-\text{O}-\text{C})$ at $\sim 1050 \text{ cm}^{-1}$, DMP $\nu(\text{P}-\text{O})$ at $\sim 1080 \text{ cm}^{-1}$, and surface methoxy $\nu_{\text{s}}(\text{C}-\text{H})$ at 2820 cm^{-1} . For simplicity, we make no distinction of the two chemically different TMP and DMP species observed on goethite in DRIFTS, and hence, we use the sum of the DMP doublet $\nu(\text{P}-\text{O})$ bands at $\sim 1080 \text{ cm}^{-1}$ and $\sim 1072 \text{ cm}^{-1}$. This has little effect on the results, since the $\nu(\text{P}-\text{O})$ is dominated by the 1080 cm^{-1} band. We use the same calibration of absorbance units ($\log(1/R)$) to absolute surface coverage as reported before (see Section 2). Denoting the surface coverage of TMP, DMP and surface methoxy θ_1 , θ_2 , and θ_3 , respectively, and assuming zero order TMP and DMP adsorption kinetics [6], the following first order rate equations are obtained:

$$\frac{d\theta_1}{dt} = k_1 - k_2\theta_1 \quad (6)$$

$$\frac{d\theta_2}{dt} = k_2\theta_1 - k_5\theta_2 \quad (7)$$

$$\frac{d\theta_3}{dt} = 2k_5\theta_2(1 - \theta_3) + k_2\theta_1(1 - \theta_3) - k_3\theta_3 - k_4\theta_3 \quad (8)$$

Here, k_1 is the rate of TMP adsorption, k_2 is the rate of methoxy displacement from TMP, k_3 is the rate of methoxy oxidation, k_4 is the rate of methanol desorption, and k_5 is the rate of DMP hydrolysis. In these simulations, we cannot separate between reactions 3 and 4 (i.e., k_3 and k_4). Contribution from reaction 3 can, however, be made by comparisons with DRIFTS data, that is, whether formate is present or not in the spectra. In contrast, we cannot conclude from the simulations whether, or to what extent, reaction 4

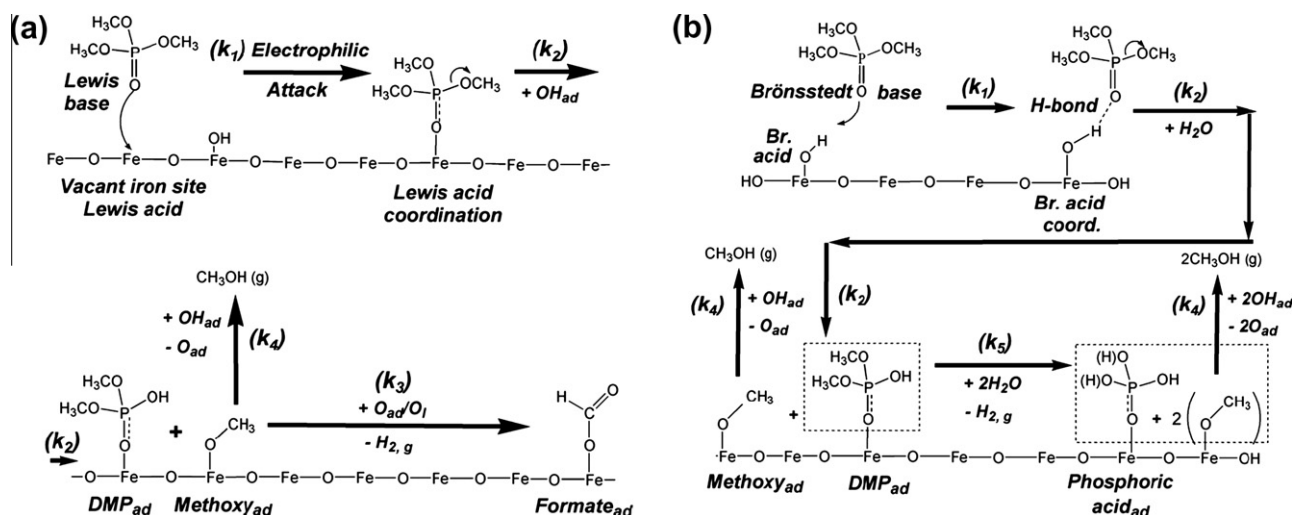


Fig. 7. (a) Proposed reaction scheme for TMP on dry hematite (maghemite) in synthetic air showing the main steps in the oxidative, surface mediated dissociation pathway. (b) Proposed reaction scheme for TMP on goethite, and water pre-covered oxide surfaces, showing the main steps in the hydrolysis pathway.

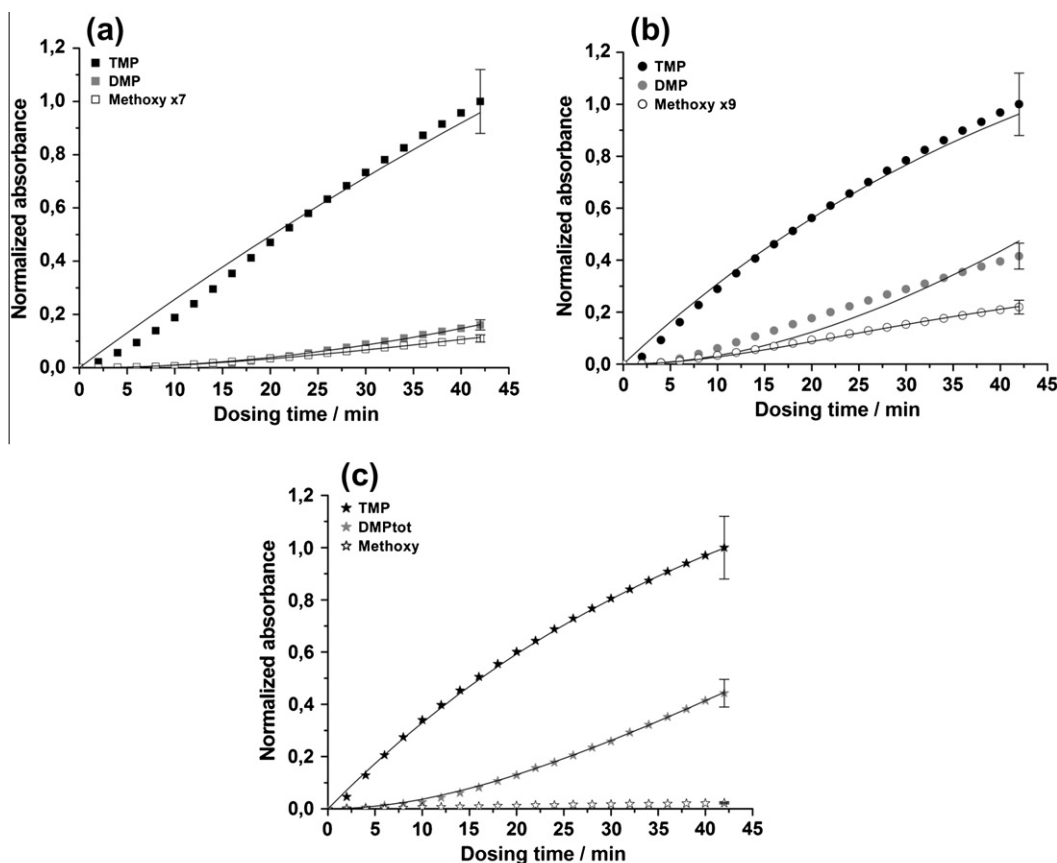


Fig. 8. Normalized absorbance due to surface TMP ($\sim 1050\text{ cm}^{-1}$), DMP ($\sim 1080\text{ cm}^{-1}$), and methoxy ($\sim 2820/2806\text{ cm}^{-1}$) as a function of TMP dosing time on (a) hematite, (b) maghemite, and (c) goethite, respectively. The experimental data are indicated by symbols, and the results from kinetic model simulations are shown by solid lines. The methoxy absorbance has been multiplied by the numerical factor indicated in each legend. The error bars represent 12% of experimental data.

contributes. We therefore report the sum ($k_3 + k_4$) from the simulations and interpret the relative importance of k_4 based on comparisons with DRIFTS data. Further, k_5 takes into account DMP decomposition by the hydrolysis reaction 5. However, in the model, we make no a priori assumption whether oxidation and hydrolysis of DMP occurs and therefore k_5 simply denotes decomposition of DMP, which may yield surface methoxy (first term in Eq. (8)).

Numerical integration of Eqs. (6)–(8), and minimizing the least square to experimental data (see Section 2), yields the solid curves in Fig. 8 for hematite, maghemite, and goethite. Assuming similar infrared cross sections, it is expected that DMP and TMP obey the same calibration based on the $\nu(P-O)$ mode analysis, and the experimental coverage of DMP is multiplied by the factor 3/2 for stoichiometric reasons. The coverage of surface methoxy is related

Table 6

Rate constants, k_i , from least square fit of DRIFTS data to kinetic model simulations for TMP adsorption on dry hematite, maghemite, and goethite nanoparticles.

Mineral	k_1	k_2	k_3	$k_4 + k_5$	rms	Methoxy scale factor ^a
Hematite	0.026	0.0052	0	0.018	0.21	5
Maghemite	0.032	0.014	0	0.039	0.28	7
Goethite ^b	0.032	0.014	0.006	–	0.16	–

^aScale factor obtained from simulations, which relates methoxy $\nu(\text{CH})$ absorbance to TMP $\nu(\text{P=O})$ absorbance.

^b Sum of DMP bands at 1080 and 1072 cm^{-1} used in the simulations.

to the TMP and DMP coverage by an unknown factor (taking into account the different cross section for the $\nu_s(\text{C-H})$ and $\nu_a(\text{C-O-P})/\nu(\text{P-O})$ vibrations) and is here used as a fitting parameter in the simulations together with the rate constants. Employing the $\nu_s(\text{C-H})$ mode, it is expected from gas-phase data that the infrared cross section for this mode is lower by approximately an order of magnitude as compared to the $\nu_a(\text{C-O-P})$ and $\nu(\text{P-O})$ modes. This is also approximately borne out in the simulations.

The results from these simulations are summarized in Table 6. First, it is evident that the rate of TMP dissociation (k_2) compared to TMP adsorption (k_1) is estimated to be $k_2/k_1 \sim 0.6$ for maghemite and goethite, and $k_2/k_1 \sim 0.3$ for hematite. On hematite and maghemite, it is found that the data are well-described by omitting DMP decomposition, that is, $k_5 = 0$, which is consistent with the absence of orthophosphate in both DRIFTS and XPS. Thus, on the dry oxides, methoxy formation originates only from cleavage of the TMP methoxy group in reaction step 2. Moreover ($k_3 + k_4$), on maghemite is ~ 2 times larger compared to hematite. Considering that the surface concentration of formate is higher on hematite than maghemite (see Fig. 1), this implies a higher rate of desorption of surface methoxy to gas-phase methanol ($k_4 \gg k_3$) on maghemite. Conversely, this indicates a stronger surface interaction with the methoxy groups on hematite compared to the other (hydr)oxides, which favors formation of surface coordinated formate species. The same analysis for goethite is, however, ambiguous due to the weak, doublet methoxy DRIFTS bands, which prohibits accurate simulations of ($k_3 + k_4$). In contrast to the oxides, description of the adsorption kinetics on goethite must include the hydrolysis reaction, that is, k_5 must be taken to be non-zero ($k_5 = 0.015 \text{ min}^{-1}$), to describe the experimental data, which takes into account that orthophosphate is formed on these samples (reaction 5), in agreement with DRIFT and XPS data. The simulations thus quantitatively support the experimental findings that orthophosphate formation on goethite occurs via a hydrolysis mechanism, which is not present (or dominant) on the oxide particles. Finally, we can now also understand why the relative concentration of DMP compared to TMP is highest on maghemite on the dry surfaces. The rate of TMP dissociation is ca. two times higher on maghemite and goethite compared to hematite. However, on goethite, hydrolysis of DMP takes place, which lowers the DMP concentration on these particles.

5. Conclusions

Adsorption and reaction of TMP and TEP on well-characterized hematite, maghemite, and goethite nanoparticles have been studied by DRIFT spectroscopy and XPS, with and without pre-adsorbed water, as a model system for OP interaction with iron (hydr)oxide minerals. On hematite and maghemite, TMP and TEP coordinate mainly to Lewis acid Fe sites through the O phosphoryl atom (P=O-Fe), while the coordination to goethite is composed of two contributions, one major contribution associated with hydrogen bonding to Brønsted acid surface OH groups and one minor

contribution from coordination to Fe sites. Methoxy is displaced from TMP on hematite and maghemite nanoparticles and results in formation of surface coordinated DMP and methoxy species. On dry hematite, methoxy is further oxidized to formate. To account for balance on maghemite and goethite, a reaction pathway that leads to desorption of gas-phase species is proposed. In contrast to hematite and maghemite, TMP dissociation on goethite occurs primarily through a surface hydrolytic pathway, which results in DMP, methanol desorption, and surface orthophosphate species. In contrast to TMP, it is found that TEP adsorbs molecularly on all nanoparticles at room temperature, and that is explained by charge stabilization due to the longer aliphatic chain.

Acknowledgments

We thank Gunnar Westin, Uppsala University, for sample preparation, and Andrey Shukaryev, Umeå University, for XPS measurements. This work was funded by Centre for Environmental Research, CMF (Grant No. 0632299), and Swedish Research Council (Grant No. 621-2006-5152).

Appendix A. Supplementary material

Supplementary data associated with this article can be found, in the online version, at <http://dx.doi.org/10.1016/j.jcis.2012.10.012>.

References

- [1] G. Ertl, H. Knözinger, J.E. Weitkamp, Handbook of Heterogeneous Catalysis, Wiley-VCH Verlag, Weinheim, 1997.
- [2] R.M. Cornell, U. Schwertmann, The Iron Oxides: Structure, Properties, Reactions, Occurrence and Uses, VCH, New York, 1996.
- [3] A.C. Garade, M. Bharadwaj, S.V. Bhagwat, A.A. Athawale, C.V. Rode, Catal. Commun. 10 (2009) 485.
- [4] C.P. Huang, Y.H. Huang, Appl. Catal. A – Gen. 346 (2008) 140.
- [5] D.L. Jones, P.G. Dennis, A.G. Owen, P.A.W. van Hees, Plant Soil 248 (2003) 31.
- [6] P. Mäkie, G. Westin, P. Persson, L. Österlund, J. Phys. Chem. A 115 (2011) 8948.
- [7] J.G. Ekerdt, K.J. Klabunde, J.R. Shapley, J.M. White, J.T. Yates, J. Phys. Chem. 92 (1988) 6182.
- [8] M.B. Mitchell, V.N. Sheinker, E.A. Mintz, J. Phys. Chem. B 101 (1997) 11192.
- [9] E.G. Garrido-Ramirez, B.K.G. Theng, M.L. Mora, Appl. Clay Sci. 47 (2010) 182.
- [10] A. Dannenberg, S.O. Pehkonen, J. Agric. Food Chem. 46 (1998) 325.
- [11] Y. Schnurer, P. Persson, M. Nilsson, A. Nordgren, R. Giesler, Environ. Sci. Technol. 40 (2006) 4145.
- [12] M.A. Henderson, T. Jin, J.M. White, J. Phys. Chem. 90 (1986) 4607.
- [13] W. Stumm, B. Sulzberger, Geochim. Cosmochim. Acta 56 (1992) 3233.
- [14] W.H. Casey, T.W. Swaddle, Rev. Geophys. 41 (2003) 1008.
- [15] R. Olsson, R. Giesler, J.S. Loring, P. Persson, Langmuir 26 (2010) 18760.
- [16] A.M. Ikaev, P.G. Mingalyov, G.V. Lisichkin, Colloid J. 69 (2007) 741.
- [17] E.A. Kozlova, P.G. Smirniotis, A.V. Vorontsov, J. Photochem. Photobiol., A 162 (2004) 503.
- [18] C.S. Kim, R.J. Lad, C.P. Tripp, Sensor. Actu., B 76 (2001) 442.
- [19] A. Waghe, S.M. Kanan, I. Abu-Yousef, B. Jensen, C.P. Tripp, Res. Chem. Intermed. 32 (2006) 613.
- [20] S.M. Kanan, C.P. Tripp, Langmuir 17 (2001) 2213.
- [21] Y.X. Li, J.R. Schlup, K.J. Klabunde, Langmuir 7 (1991) 1394.
- [22] M.A. Henderson, J. Phys. Chem. C 115 (2011) 23527.
- [23] D.A. Trubitsyn, A.V. Vorontsov, J. Phys. Chem. B 109 (2005) 21884.
- [24] A. Kiselev, A. Mattson, M. Andersson, A.C.E. Palmqvist, L. Österlund, J. Photochem. Photobiol., A 184 (2006) 125.
- [25] L. Österlund, V. Stengl, A. Mattsson, S. Bakardjieva, P.O. Andersson, F. Oplustil, Appl. Catal., B 88 (2009) 194.
- [26] N.J. Harrick, Internal Reflection Spectroscopy, Harrick Scientific Corporation, New York, 1987.
- [27] S. Morita, 2Dshige (c), Kwansei-Gakuin University, 2004–2006.
- [28] I. Noda, Y. Ozaki, Two-Dimensional Correlation Spectroscopy. Applications in Vibrational and Optical Spectroscopy, Wiley, Chichester, 2004.
- [29] A. Bengtsson, A. Shchukarev, P. Persson, S. Sjöberg, Geochim. Cosmochim. Acta 73 (2009) 257.
- [30] S.R. Segal, L.X. Cao, S.L. Suib, X. Tang, S. Satyapal, J. Catal. 198 (2001) 66.
- [31] J. Florián, V. Baumruk, M. Šýtrajbl, L. Bednárová, J. Šýtěpánek, J. Phys. Chem. 100 (1996) 1559.
- [32] Y.F. Guan, C.J. Wurrey, G.J. Thomas, Biophys. J. 66 (1994) 225.
- [33] J.A. Moss, S.H. Szczepankiewicz, E. Park, M.R. Hoffmann, J. Phys. Chem. B 109 (2005) 19779.
- [34] C. Cao, K.L. Hohn, Appl. Catal., A 354 (2009) 26.
- [35] S.D. Lin, H.K. Cheng, T.C. Hsiao, J. Mol. Catal. A – Chem. 342–43 (2011) 35.

- [36] C.N. Rusu, J. Yates, J. Phys. Chem. B 104 (2000) 12292.
[37] S. Bailey, G.F. Froment, J.W. Snoeck, K.C. Waugh, Catal. Lett. 30 (1995) 99.
[38] J. Rasko, T. Kecskes, J. Kiss, J. Catal. 224 (2004) 261.
[39] G. Busca, J. Lamotte, J.-C. Lavalley, V. Lorenzelli, J. Am. Chem. Soc. 109 (1987) 5197.
[40] A. Glisenti, J. Chem. Soc. Faraday Trans. 94 (1998) 3671.
[41] D.A. Chen, J.S. Ratliff, X. Hu, W.O. Gordon, S.D. Senanayake, D.R. Mullins, Surf. Sci. 604 (2010) 574.
[42] D.A. Trubitsyn, A.V. Vorontsov, Mendeleev Commun. 14 (2004) 197.
[43] G. Lefèvre, Adv. Colloid. Interface 107 (2004) 109.
[44] P. Persson, N. Nilsson, S. Sjöberg, J. Colloid. Interface. Sci. 177 (1996) 263.
[45] J. Stangre, R. Savoie, Can. J. Chem. 70 (1992) 2875.
[46] A. Siokou, R.M. Nix, J. Phys. Chem. B 103 (1999) 6984.
[47] N. Tarrat, J. Mol. Struct. – Theochem 941 (2010) 56.
[48] A. Dmitry, A.V. Vorontsov, J. Phys. Chem. B 109 (2005) 21884.
[49] V.N. Scheinker, M.B. Mitchell, Chem. Mater. 14 (2002) 1257.